

Transport and spectroscopic signatures of a disorder stabilized metal in two-dimensional frustrated Mott insulators

Madhuparna Karmakar^{1,*} and Nyayabanta Swain^{2,†}

¹*Department of Physics, Indian Institute of technology, Madras, Chennai-600036, India.*

²*Centre for Quantum Technologies, National University of Singapore, Singapore 117543.*

(Dated: June 14, 2022)

Frustrated Mott insulators such as, transition metal dichalcogenides present an ideal platform for the experimental realization of externally tuned insulator-metal transition. In this paper we present the first non perturbative numerical investigation of the disorder induced insulator-metal transition in a two-dimensional frustrated Mott insulator. Our approach is generic and captures the essential physics of Mott insulator-metal transition in geometrically frustrated lattices. For concreteness, we have compared our results with the experimental observations on copper (Cu) intercalated 1T-TaS₂. Based on the magnetic, spectroscopic and transport signatures we have mapped out the thermal phase diagram of Cu intercalated 1T-TaS₂ and established that over a regime of moderate disorder strength this material hosts an antiferromagnetic metal. Moreover, the insulator-metal transition in this system is not tied to the loss of magnetic correlations, thereby giving rise to two quantum critical points. The emergent non Fermi liquid metal is governed by resilient quasiparticles, that survive as the relevant low energy excitations even after the break down of the Fermi liquid description. The transport and spectroscopic signatures discussed in this letter are expected to serve as important benchmarks for future experiments on this and related class of materials.

I. INTRODUCTION

Interplay of interaction and disorder in systems with strong electron-electron correlation has always been a subject of fundamental interest in condensed matter physics¹⁻³. In the non interacting limit, an infinitesimal disorder is known to lead to Anderson localization in one and two dimensions, while a three dimensional system undergoes a metal-insulator transition (MIT) at a critical disorder strength^{4,5}. In the opposite limit are the Mott insulators wherein strong electron-electron interaction leads to localization at commensurate electron filling⁶. At low temperatures, Mott insulators are often associated with magnetic ordering, low energy spin excitations and gapped charge excitations^{7,8}. The outcome of the interplay between these two localizing tendencies was suggested to stabilize a metallic phase between the Mott and the Anderson insulating phases, leading to an insulator-metal-insulator transition, in two-dimensions (2D)^{9,10}. The first possibility of a Mott insulator-metal transition (IMT) in 2D was suggested based on the renormalization group (RG) theory by Finkel'stein^{9,10}, while the first experimental signature of the same was observed in the transport data of high mobility silicon metal oxide semiconductor field effect transistor^{2,11}.

Disorder induced IMT on the bipartite square lattice is an well investigated subject, both at the ground state and at finite temperatures. The range of applied theoretical tools include, inhomogeneous mean field theory^{12,13}, dynamical mean field theory (DMFT) and its variants¹⁴⁻²⁴, determinant quantum Monte Carlo (DQMC)²⁵⁻²⁷, exact diagonalization²⁸, typical medium theory²⁹ and its extensions³⁰, auxiliary field quantum Monte Carlo with static path approximation³¹ etc. In the clean limit this system is a Mott insulator with a Neel antiferromagnetic order of the local moments. Disorder brings electron itinerancy back into the picture, thereby allowing the competition between insulating tendency of the localized moments and the metallicity of the itinerant electrons. The outcome of this competition is a metallic regime which lacks any mag-

netic ordering, at intermediate disorder. Notably, the system hosts a single quantum critical point (QCP) corresponding to the IMT; the onset of metallicity is accompanied by the loss of (quasi) long range magnetic order³¹.

The primary difficulty in the experimental realization of IMT is to find suitable Mott insulators in which disorder can be introduced in a controlled manner without changing the carrier concentration. An avenue to circumvent this difficulty is the recently discovered 2D transition metal dichalco-

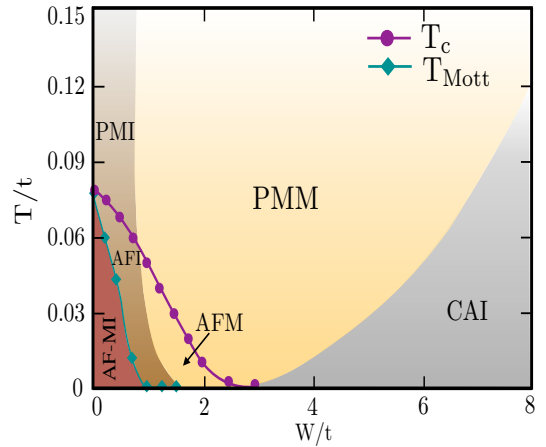


FIG. 1. Color online: Phase diagram of Anderson-Hubbard model on a triangular lattice in the disorder-temperature ($W - T$) plane at $U = 6t$. Different phases of this model are antiferromagnetic gapped Mott insulator (AF-MI), antiferromagnetic gapless insulator (AFI), antiferromagnetic metal (AFM), paramagnetic insulator (PMI), paramagnetic metal (PMM) and the non magnetic correlated Anderson insulator (CAI). The thermal scales T_{Mott} and T_c indicate the temperatures where the Mott gap and the magnetic correlations vanish, respectively. See text for detail characterization of the phases.

genide (TMD) and related systems, which allows for the independent control over lattice filling and electron-electron correlations^{32,33}. One such candidate material is 1T-TaS₂, which is a geometrically frustrated system with a rich phase diagram^{34–38}. Recent experiments on intercalation of 1T-TaS₂ with potassium (K)³⁹, copper (Cu)⁴⁰ and iron (Fe)⁴¹ have brought forth the possibility of IMT and a disorder stabilized “magnetic” metal in this material; the origin of the same is currently debated^{39,42,43}.

Geometric frustration dictates the low temperature magnetic state both in clean and disordered systems^{44,45}. In presence of frustration the (quasi) long range magnetic order is not tied to the IMT and the magnetic correlations survive even after the Mott gap collapses. The system thus hosts different QCPs corresponding to the IMT and the loss of magnetic order. Multiple QCPs is a generic feature of geometrically frustrated lattices and has been observed in recent experiments on 2D TMDs³³. This is in sharp contrast with the bipartite lattices wherein IMT is tied to the loss of the magnetic order, leading to a single QCP³¹. Note that at low temperatures the magnetic order is closely tied to the lattice geometry as long as the disorder strength is comparable to the electron correlation.

In this paper we report the first non perturbative theoretical study of disorder induced IMT in 2D frustrated Mott insulators. While our approach and results are generic for such systems, for concreteness we present the example of Cu intercalated 1T-TaS₂ and compare our results with the relevant experimental observations made on this material. The tool of our choice is auxiliary field quantum Monte Carlo technique with static path approximation (SPA)⁴⁶, which has been extensively utilized in the context of magnetic and superconducting systems^{47–54} (see appendix). Recently SPA has also been used to investigate disorder induced IMT in square lattice; the results obtained therein are in agreement with the existing understanding of IMT in unfrustrated lattices^{12–24,27–30,55}.

Our key results on disorder induced IMT in 2D frustrated Mott insulators are as follows: (i) We map out the generic thermal phase diagram to show the disorder induced IMT in 2D frustrated Mott insulator, wherein a metallic phase is stabilized over a regime of intermediate disorder potential. (ii) Owing to the geometric frustration the system hosts separate QCPs corresponding to the IMT and loss of (quasi) long range magnetic order. (iii) The disorder stabilized emergent *antiferromagnetic* metal is a non Fermi liquid (NFL), characterised by resilient quasiparticles (QP), as attested via the transport and spectroscopic signatures. (iv) The metallic phase exhibits a thermal crossover between NFL and bad metallic phases as a re-entrant thermal transition, characterized by a change in the sign of $d\sigma_{dc}/dT$ (T is temperature and σ_{dc} is dc conductivity, discussed later). (v) Our results provide the first microscopic description of the existing experimental observations on Cu intercalated 1T-TaS₂ and serves as benchmarks for related class of materials.

II. MODEL AND METHOD

We model the disordered 2D frustrated Mott insulator as the Anderson Hubbard model on a triangular lattice⁸, which reads as,

$$H = \sum_{\langle ij \rangle, \sigma} t_{ij} c_{i\sigma}^\dagger c_{j\sigma} + h.c. + \sum_{i, \sigma} (W_i - \mu) \hat{n}_{i\sigma} + U \sum_i \hat{n}_{i\uparrow} \hat{n}_{i\downarrow}$$

here, $t_{ij} = -t$, for the nearest neighbor hoppings on an isotropic triangular lattice (coordination number $z = 6$). $t = 1$ is set as the reference energy scale. $U > 0$ is the on-site repulsive Hubbard interaction. The site dependent disorder is introduced in the system via W_i which is randomly selected from an uniform distribution $[+W/2, -W/2]$. We work at half filling and the chemical potential μ is adjusted to achieve the same.

We make this model numerically tractable by decomposing the interaction term via Hubbard Stratonovich (HS) decomposition^{56,57}, which introduces a vector $\mathbf{m}_i(\tau)$ and a scalar $\phi_i(\tau)$ (bosonic) auxiliary field at each site, where the former couples to the spin and the later to the charge. We next drop the time dependence of these auxiliary fields and treat them as “classical” fields \mathbf{m}_i and ϕ_i . The thermal fluctuations in \mathbf{m}_i are retained completely but ϕ_i is treated at the saddle point level, $\phi_i \rightarrow \langle \phi_i \rangle = \langle n_i \rangle U/2$. These approximations lead to a coupled spin-fermion model wherein the fermions move in the spatially fluctuating background of \mathbf{m}_i . The equilibrium configurations of $\{\mathbf{m}_i\}$ are generated via Monte Carlo (MC) simulation and the different correlators are computed on these equilibrium configurations. Technical details of the method are discussed in the appendix.

III. RESULTS

The different phases of this system are characterized by the following indicators:

- Magnetic structure factor,

$$S(\mathbf{q}) = \frac{1}{N^2} \sum_{ij} \langle \mathbf{m}_i \cdot \mathbf{m}_j \rangle e^{i\mathbf{q} \cdot (\mathbf{r}_i - \mathbf{r}_j)} \quad (1)$$

where, \mathbf{q} corresponds to the magnetic ordering wave vector and N is the number of lattice sites. $\langle \dots \rangle$ corresponds to MC configurational average.

- Single particle density of states (DOS),

$$N(\omega) = (1/N) \sum_{\alpha} \langle \delta(\omega - \epsilon_{\alpha}) \rangle \quad (2)$$

where, ϵ_{α} are eigenvalues in a single equilibrium configuration.

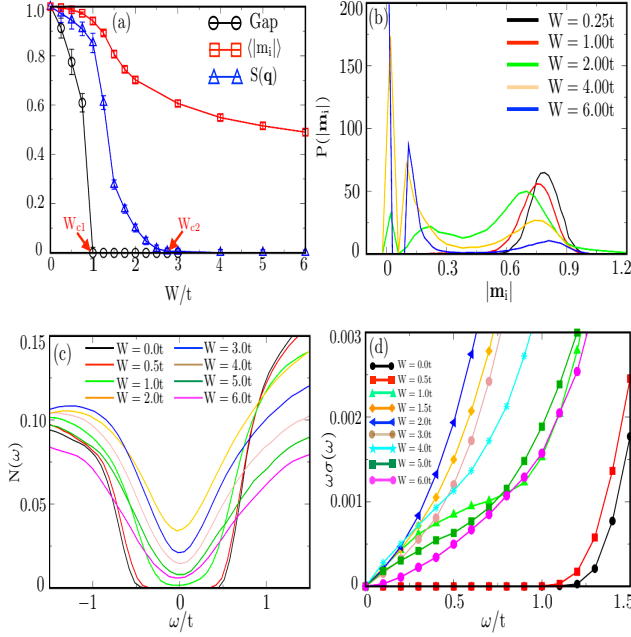


FIG. 2. Color online: (a) Disorder dependence of normalized single particle energy gap, (Gap), normalized magnetic moment amplitude ($\langle |m_i| \rangle$) and normalized magnetic structure factor peak ($S(\mathbf{q})$), at $T = 0$. The error bars correspond to the cumulative error arising out of MC and disorder averaging of the observables. (b) Distribution of magnetic moments ($P(|\mathbf{m}_i|)$) at $T = 0$ for different disorder potentials. Note the transfer of weight towards $|\mathbf{m}_i| = 0$ with increasing disorder, indicating the spatial fragmentation of the system into puddles with suppressed amplitude of local moments, followed by the percolation of these puddles. (c) Single particle DOS ($N(\omega)$) as function of disorder at $T = 0$. (d) Scaled optical conductivity ($\omega\sigma(\omega)$) (in appropriate units) plotted over a small range of low frequencies, for different disorder potential, at $T = 0$.

- Single particle local density of states (LDOS),

$$\rho_i(\omega) = \sum_{\alpha, \sigma} \langle |u_{\alpha, \sigma}^i|^2 \delta(\omega - \epsilon_\alpha) \rangle \quad (3)$$

where, $u_{\alpha, \sigma}^i$ is the eigenvector corresponding to the eigenvalue ϵ_α .

- Inverse participation ratio (IPR),

$$IPR = \frac{\sum_{i, \alpha, \sigma} |u_{\alpha, \sigma}^i|^4}{[\sum_{i, \alpha, \sigma} |u_{\alpha, \sigma}^i|^2]^2} \quad (4)$$

- Optical conductivity, calculated using the Kubo formula,

$$\sigma(\omega) = \frac{\sigma_0}{N} \sum_{\alpha, \beta} \frac{n_\alpha - n_\beta}{\epsilon_\beta - \epsilon_\alpha} \langle |\alpha| J_x |\beta\rangle|^2 \delta(\omega - (\epsilon_\beta - \epsilon_\alpha)) \quad (5)$$

where, the current operator J_x is defined as,

$$J_x = -i \sum_{i, \sigma, \delta} [\delta_{\delta}^{\dagger} c_{\mathbf{r}_i, \sigma}^{\dagger} c_{\mathbf{r}_i + \vec{\delta}, \sigma} - h.c] \quad (6)$$

The dc conductivity (σ_{dc}) is the $\omega \rightarrow 0$ limit of $\sigma(\omega)$, $\sigma_0 = \frac{\pi e^2}{h}$ in 2D. $n_\alpha = f(\epsilon_\alpha)$ is the Fermi function, and ϵ_α and $|\alpha\rangle$ are respectively the single particle eigenvalues and eigenvectors of H_{eff} in a given background of $\{\mathbf{m}_i\}$.

- Spectral line shape,

$$A(\mathbf{k}, \omega) = -(1/\pi) \text{Im}G(\mathbf{k}, \omega) \quad (7)$$

where, $G(\mathbf{k}, \omega) = \lim_{\delta \rightarrow 0} G(\mathbf{k}, i\omega_n)|_{i\omega_n \rightarrow \omega + i\delta}$. $G(\mathbf{k}, i\omega_n)$ is the imaginary frequency transform of $\langle c_{\mathbf{k}}(\tau) c_{\mathbf{k}}^{\dagger}(0) \rangle$.

The results presented here corresponds to a system size of 24×24 and are found to be robust against finite system size effects (see appendix). The on-site Hubbard repulsion is selected to be $U = 6t$ which is close to the Mott boundary of the triangular lattice in the clean limit^{22,23,35,49,58-71}. This choice of U ensures that our parameter regime is well suited to capture the experimental observations on Cu intercalated 1T-TaS₂^{37,40}. The observables are averaged over 30 disorder realizations.

A. Phase diagram and thermal scales

In the clean limit, the half filled triangular lattice at $U = 6t$ hosts a 120° spiral magnetic order with the ordering wave vector $\mathbf{Q} = \{2\pi/3, 2\pi/3\}$, in the ground state^{22,23,35,49,58-69}. The corresponding antiferromagnetic Mott insulator (AF-MI) phase undergoes thermal transition to a paramagnetic insulator (PMI) comprising of randomly oriented magnetic moments⁴⁹. Introduction of quenched random disorder alters this picture significantly and leads to a disorder induced IMT, as shown in Figure 1. We characterize the resulting phases based on the indicators shown in Figure 2. The regime of weak disorder ($0 < W \lesssim t$) is akin to the clean limit and hosts an AF-MI in the ground state, comprising of a robust spectral gap at the Fermi level. Increasing disorder leads to progressive accumulation of spectral weight at the Fermi level such that the Mott gap collapses for $W \geq t$, even though the magnetic order survives. The collapse of the Mott gap sets the first QCP ($W_{c1} \sim t$) of the system, while a second QCP ($W_{c2} \sim 2.75t$) is set by the loss of the magnetic order. We show these QCPs in Figure 2(a), as disorder dependence of Mott gap and magnetic structure factor peaks, respectively. In addition, we show the disorder dependence of the average local moment amplitude ($\langle |m_i| \rangle$), which survives even at strong disorder. The system does not undergo any spontaneous symmetry breaking across the disorder induced quantum phase transitions. The order of these transitions are reminiscent of weak first order transition observed in the clean limit⁷²⁻⁷⁴.

The distribution of the average magnetic moment amplitude ($P(|\mathbf{m}_i|)$) is shown in Figure 2(b). At weak disorder $P(|\mathbf{m}_i|)$ is unimodal indicating a homogeneous distribution of local moments with a mean amplitude of \bar{m} . Increase in disorder results in progressive fragmentation of the magnetic state indicated by the broadening of the peak. Along with \bar{m} there is accumulation of weight at $|\mathbf{m}_i| = 0$ which indicates that the system comprises of regions with vanishing local moment amplitude.

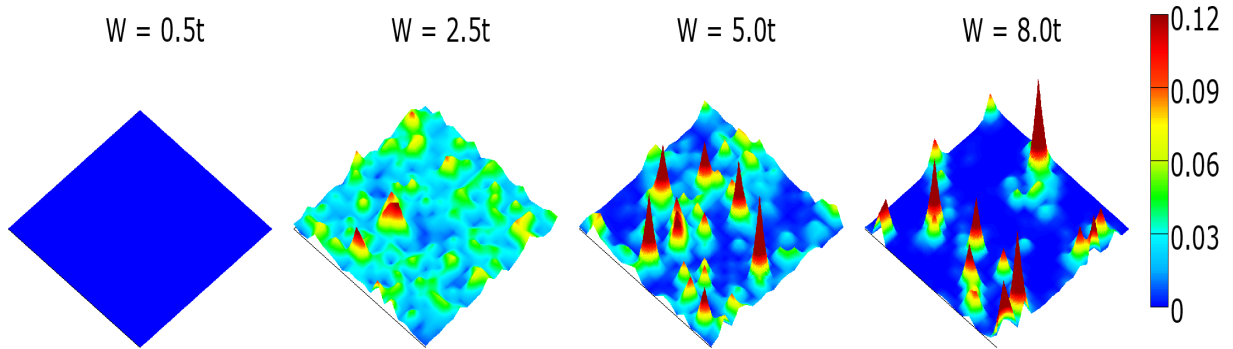


FIG. 3. Color online: Spatial maps of local density of states ($N_i(0)$) at the Fermi level at different disorder potential across the insulator-metal-insulator transition. While both AF-MI and CAI are characterized by localized energy states, the AFM regime shows significant delocalization of the energy states (see text).

The intermediate disorder regime shows that the contributions from \bar{m} and $|\mathbf{m}_i| = 0$ are comparable. On further increasing disorder the regimes with suppressed magnetic moments percolate through the system, thereby destroying the magnetic order. The corresponding $P(|\mathbf{m}_i|)$ shows that the weight is now largely accumulated at $|\mathbf{m}_i| = 0$.

In Figure 2(c) we show the single particle DOS at the ground state for a range of disorder potentials. While the AF-MI comprises of a robust spectral gap, the antiferromagnetic insulator (AFI), antiferromagnetic metal (AFM) and correlated Anderson insulator (CAI) shown in Figure 1 are gapless phases and can not be distinguished based on the single particle DOS alone. The distinction is made based on the transport properties of the system. Transport signature of the system is shown in Figure 2(d) in terms of the scaled optical conductivity ($\omega\sigma(\omega)$). For $W \leq W_{c1}$, $\omega\sigma(\omega) = 0$, corresponding to a gapped AF-MI. Over a narrow regime $W_{c1} \leq W < 1.50t$, $\omega\sigma(\omega) \rightarrow 0$ as $\omega \rightarrow 0$, *nonlinearly*, indicating an insulating phase⁷⁵. In the regime $1.50t < W \leq W_{c2}$, $\omega\sigma(\omega) \rightarrow 0$ *linearly*, thus, $\sigma(\omega)$ is a constant at small ω , corresponding to a metal.

B. Disorder induced localization

The regime $W > W_{c2}$ of Figure 1 corresponds to the CAI, characterized by the absence of magnetic order, presence of gapless excitations and localized low energy single particle eigenstates. In Figure 3 we show the localization of the single particle states at the representative disorder strengths, in terms of the LDOS at the Fermi level. In the AF-MI phase LDOS is gapped, at $W = 2.5t$ the system is an AFM, characterized by the delocalized energy states as shown in the LDOS maps. The system is in the CAI phase both at $W = 5t$ and at $W = 8t$, and the corresponding LDOS maps show progressively robust localization of the energy states. At still stronger disorder (not shown here) the energy states at the Fermi level gets completely localized via Anderson localization phenomenon.

In Figure 4(a) we show the inverse participation ratio (IPR) and the dc conductivity (σ_{dc}) at the ground state, that have

been used to characterize the CAI phase. The localization length (ξ_{loc}) of an eigenstate $\psi_{i,\alpha}$ is related to the IPR as, $IPR \propto \xi_{loc}^{-2}$; consequently, increase in disorder is expected to reduce ξ_{loc} and increase IPR. The disorder dependence of IPR at the Fermi level shown in Figure 4(a) corresponds to the results at the thermodynamic limit, determined based on the finite system size scaling analysis of IPR, shown in Figure 4(b). Our result suggests that for both AF-MI and CAI, the IPR increases with increasing disorder. The disorder regime $W_{c1} < W \leq 1.50t$ corresponding to the AFI is weakly localized and has a small but finite IPR at the Fermi level. The intermediate disorder regime ($1.50t < W \leq W_{c2}$) is anomalous and an increase in disorder leads to delocalization of the eigenstates. In the thermodynamic limit, as shown in Figure 4(a), IPR vanishes over this regime of intermediate disorder potential, as is expected from a metallic phase. The anomaly in IPR over the regime $W_{c1} \leq W < W_{c2}$ is reflected in transport signatures as well, in terms of significant increase in σ_{dc} , attesting an AFI and a metallic phase.

C. Finite temperature scales

Figures 5(a)-(b) correspond to the indicators based on which the thermal scales shown in Figure 1 are determined. Figure 5(a) shows the thermal evolution of the magnetic structure factor peak ($S(\mathbf{Q})$) at different disorder potentials. The point of inflection of these curves correspond to the T_c , which undergoes suppression with increasing disorder. Note that as per the Mermin-Wagner theorem in 2D the system can not host any long range order at $T > 0$ ⁷⁶. The low temperature magnetic state observed in this system is (quasi) long range ordered; it comprises of magnetic correlations which decay as power law, unlike the exponential decay one would expect from a true disordered phase. Increase in temperature and the associated thermal fluctuations lead to progressive suppression of this “algebraic long range order” such that at high temperatures the correlations are short ranged and exponentially decaying.

The thermal evolution of the single particle DOS at the

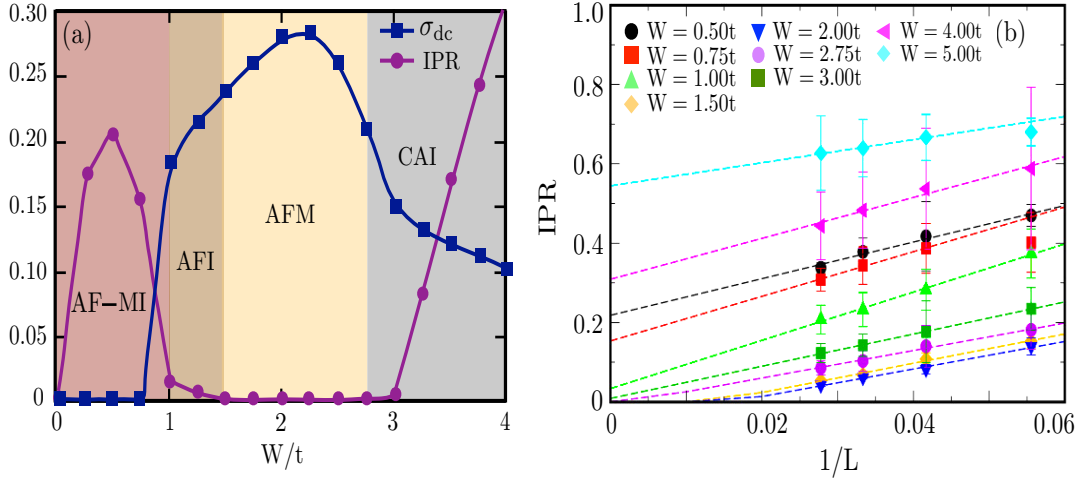


FIG. 4. Color online: (a) Disorder dependence of Inverse participation ratio (IPR) at the Fermi level in the thermodynamic limit and dc conductivity (σ_{dc}) at $L = 24$, at $T = 0$. (b) Finite system size scaling of IPR at the Fermi level at indicated disorder potentials. The points represent the numerical data. Dashed lines are linear fit to the data. The IPR vanishes for metal and extrapolates to a finite value for the insulating phase as $L \rightarrow \infty$.

Fermi level ($N(0)$) is shown in Figure 5(b), based on which T_{Mott} is determined. For a given disorder potential, temperature leads to fluctuation of magnetic moments and accumulation of spectral weight at the Fermi level. The high temperature phase is thus a paramagnetic insulator (PMI) for $W < 1.50t$, and a paramagnetic metal (PMM) for $W \geq 1.50t$. Note that $dN(0)/dT$ undergoes a temperature dependent change in sign in the regime $W_{c1} \leq W < W_{c2}$, indicating a weak “re-entrant” thermal transition.

The finite temperature metal-insulator boundaries of our phase diagram are determined based on the behavior of $\omega\sigma(\omega)$ in the low frequency regime, shown in Figure 6. At $W = 0.25t$, even at high temperatures the accumulation of weight in the low frequency regime is insignificant and the system continues to remain gapped. This high temperature regime corre-

sponds to a PMI characterized by randomly oriented magnetic moments and a spectral gap at the Fermi level. At $W = t$ the system is in the AFI phase at low temperature which is signalled by the non linear behavior of $\omega\sigma(\omega) \rightarrow 0$ as $\omega \rightarrow 0$. Increase in temperature leads to crossover of the system to a metallic phase and accordingly the low frequency behavior of $\omega\sigma(\omega)$ progressively becomes linear. The phase at $W = 2t$ is an AFM, the corresponding $\omega\sigma(\omega) \rightarrow 0$ linearly as $\omega \rightarrow 0$. The metallic regime both at low and at high temperatures is characterized by the linear low frequency dependence of $\omega\sigma(\omega)$. The insulating CAI phase at $W = 6t$ is once again signalled by the non linear behavior of $\omega\sigma(\omega) \rightarrow 0$ in the low frequency regime. For $T \gtrsim 0.1t$ the linear frequency dependence of $\omega\sigma(\omega)$ signals a finite temperature insulator-metal (CAI-PMM) crossover.

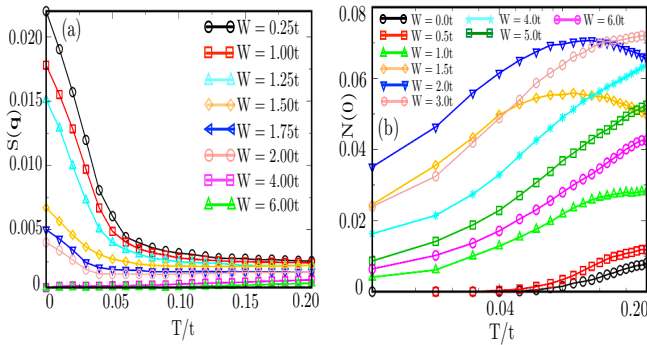


FIG. 5. Color online: (a) Thermal evolution of magnetic structure factor peak, $S(\mathbf{q})$ and (b) single particle DOS at the Fermi level, $N(0)$, at different disorder potentials.

D. Non Fermi liquid metal and thermal crossover

In order to obtain a deeper insight into the characteristics of the metallic regime at intermediate disorder potentials we next analyze the high frequency behavior of $\sigma(\omega)$, as shown in Figure 7(a), at $T = 0.06t$. Based on $\sigma(\omega)$ the different disorder regimes are characterized as follows: (i) AF-MI at weak disorder is gapped at the Fermi level, $\sigma(\omega)$ contains displaced Drude peak (DDP) at $\omega \neq 0$; (ii) moderate disorder closes the gap via spectral weight accumulation and DDP shifts to low frequencies, indicating an IMT; (iii) strong disorder leads to CAI phase and accordingly DDP shifts back to higher ω . The corresponding single particle DOS is shown in Figure 7(b). As the system undergoes transition from the AF-MI to the AFM state with increasing disorder, $N(\omega)$ accumulates large spectral weight at the Fermi level, indicating a *pseudogap* behavior. Note that similar pseudogap behavior have been observed

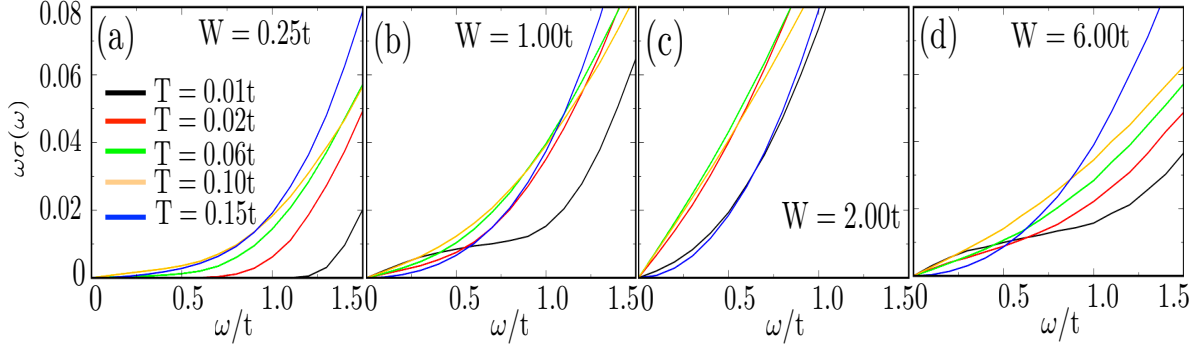


FIG. 6. Color online: Thermal evolution of scaled optical conductivity ($\omega\sigma(\omega)$) at selected disorder cross sections. A nonlinear dependence of $\omega\sigma(\omega) \rightarrow 0$ as $\omega \rightarrow 0$ indicates an insulating behavior, while for a metal the dependence is linear.

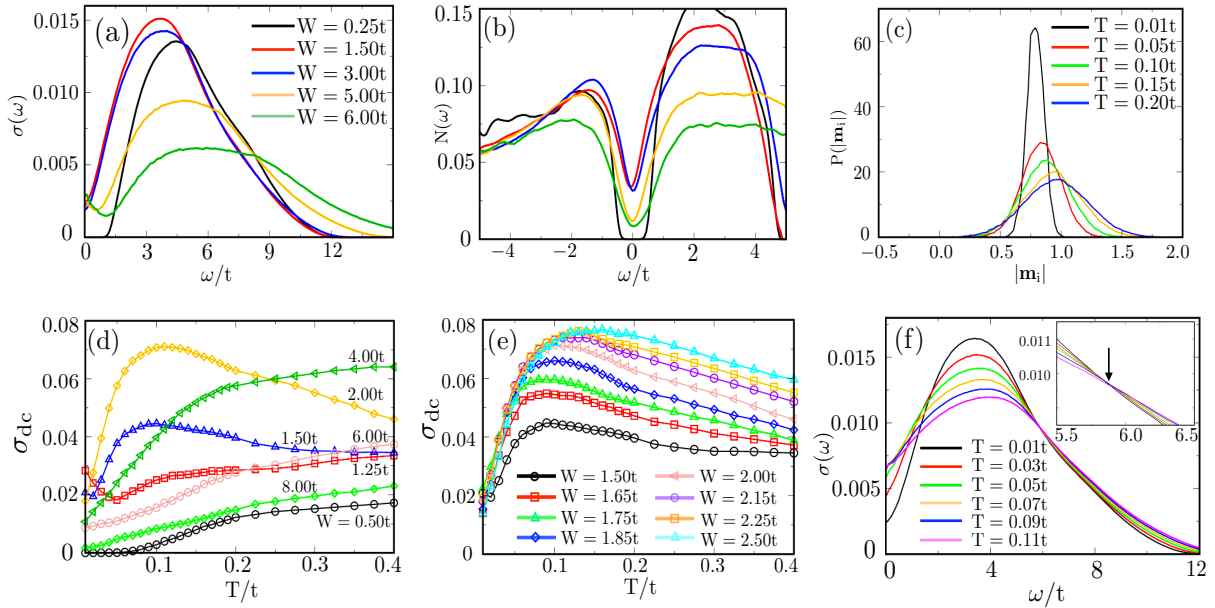


FIG. 7. Color online: (a) Optical conductivity ($\sigma(\omega)$) and (b) single particle DOS ($N(\omega)$) at different disorder potential at $T = 0.06t$. (c) Thermal evolution of the magnetic moment distribution profiles ($P(|\mathbf{m}_i|)$) at $W = 0.25t$. (d) Thermal evolution of dc conductivity (σ_{dc}) at different disorder cross sections. The NFL regime at intermediate disorders is shown in detail in (e). (f) Thermal evolution of optical conductivity at $W = 1.75t$. Inset: isosbestic crossing point ($\omega \sim 5.8t$) corresponding to thermal crossover from NFL to bad metallic phase.

in DQMC studies of disorder induced IMT on square lattice²⁷. The transition from the AFM to the CAI phase is signalled by the loss of spectral weight at the Fermi level as shown in Figure 7(b).

In Figure 7(c) we present the temperature dependence of magnetic moment distribution ($P(|\mathbf{m}_i|)$), at a selected disorder potential of $W = 0.25t$. The generic effects of temperature at any disorder cross section are, (i) suppression of the peak height of $P(|\mathbf{m}_i|)$ and (ii) shifting of \bar{m} towards larger values, with increasing temperature. This thermal dependence of $|\mathbf{m}_i|$ arises because temperature destroys angular correlations and therefore suppresses $P(|\mathbf{m}_i|)$; moreover, thermal fluctuations enhance \bar{m} but lead to a broader distribution showing that the

underlying state is not magnetically ordered. Had the underlying state been ordered, this increase in \bar{m} would have strengthened the order and made the spectral gap robust. However, in the absence of any order, magnitude fluctuations and loss of angular correlation leads to accumulation of spectral weight at the Fermi level. This increases $N(0)$ and gives rise to a pseudogap. At even higher temperatures the increase in \bar{m} slows down as shown in Figure 7(c), also the orientational fluctuations almost saturates; this leads to loss of spectral weight at the Fermi level and $N(0)$ undergoes suppression.

From the low frequency ($\omega \rightarrow 0$) behavior of $\sigma(\omega)$ we determine σ_{dc} , and show its thermal evolution in Figure 7(d). We distinguish the metallic and insulating phases primarily

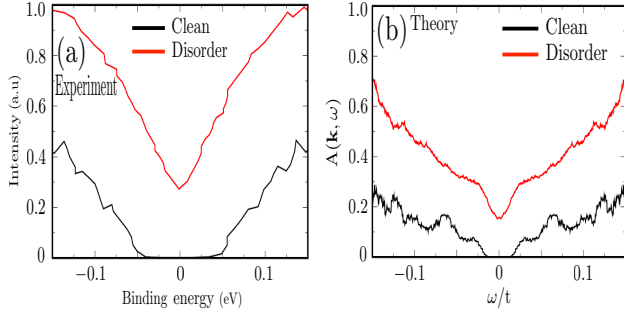


FIG. 8. Color online: (a) Symmetrized experimental energy distribution curve (EDC) determined from ARPES measurement on clean and Cu intercalated 1T-TaS₂, at the Γ -point; data extracted from⁴⁰. (b) Symmetrized spectral line shape $A(\mathbf{k}, \omega)$ as determined numerically at a low temperature for the clean ($W = 0$) and disordered ($W = 1.75t$) cases at the Γ -point of the Brillouin zone.

based on the sign of $d\sigma_{dc}/dT$, such that, $d\sigma_{dc}/dT < 0$ corresponds to metal while for an insulator $d\sigma_{dc}/dT > 0$. At high temperatures, $d\sigma_{dc}/dT > 0$ for the AF-MI ($W = 0.5t$), AFI ($W = 1.25t$) and CAI ($W = 4t, 6t, 8t$) phases and σ_{dc} increases monotonically. In the intermediate disorder regime ($W = 1.5t, 2t$) representative of the AFM, $d\sigma_{dc}/dT$ undergoes a change in sign across a crossover temperature at which σ_{dc} is maximum, say, T_{IRM} . In Figure 7(e) we explore the metallic phase at the intermediate disorder regime, in detail. The non-monotonic temperature dependence of σ_{dc} and the corresponding deviation of resistivity ($\rho = 1/\sigma_{dc}$) from the $\rho \propto T^2$ behavior at low temperatures is the signature of the underlying NFL state. The “pseudogap” behavior of the single particle DOS (Figure 7(b)) at the Fermi level suggests that even though the Fermi liquid description breaks down in the NFL state, the low energy excitations can still be described via the QPs. For $T \neq 0$ the finite spectral weight at the Fermi level progressively increases upto T_{IRM} , corresponding to the Ioffe-Regel-Mott limit^{77,78}. The NFL regime can be inferred in terms of “resilient quasiparticles”, which continues to survive as the relevant low energy excitations in the system even after the Fermi liquid description breaks down⁷⁹.

The breakdown of resilient QP description is signalled by two characteristics of $\sigma(\omega)$: (i) the DDP is broadened, undergoes suppression and gets monotonically shifted towards the high frequency range, (ii) the isosbestic crossing point of the $\sigma(\omega)$ curves is lost. We show these characteristics in Figure 7(f), where thermal evolution of $\sigma(\omega)$ is presented at a fixed disorder strength of $W = 1.75t$. The isosbestic crossing point for this disorder is at $\omega \sim 5.8t$ and is lost for $T > 0.09t$ (see inset). The thermal evolution of $\sigma(\omega)$ thus encodes signature of resilient QP phase over the regime $T \leq T_{IRM}$ and its subsequent crossover to the “bad metallic” phase for $T > T_{IRM}$. The crossover from the resilient QP to bad metal is a gradual degradation of the QP signatures and is not associated with any sharp transition. The QP energy scale given by the Brinkmann-Rice scale is tied to T_{IRM} at which the QP description breaks down.

IV. DISCUSSIONS

Resistivity measurements on Cu intercalated 1T-TaS₂ shows $d\rho/dT < 0$ in the metallic regime at low temperatures⁴⁰, in agreement with our results. Further experimental works on this and related class of systems are however called for, particularly optical measurements which provide unambiguous evidence of NFL physics. For example, signatures of NFL state and resilient QPs observed in optical measurements has recently been reported in molecular charge transfer salt κ -[(BEDT-STF)_x(BEDT-TTF)_{1-x}]₂Cu₂(CN)₃, which undergoes chemical substitution induced IMT⁸⁰. Similarly, emergence of NFL metal via the interplay of quenched disorder and strong correlation has been recently observed in x-ray irradiated organic Mott insulator κ -(ET)₂Cu[N(CN)₂]Cl^{45,81}. The emergent novel electronic state close to the Mott boundary, as identified based on nuclear magnetic resonance (NMR) measurements, is suggested to be possibly the first experimental evidence of the much sought after “electronic Griffiths phase”⁸².

In Cu intercalated 1T-TaS₂ disorder stabilized metallic regime has been reported based on the ARPES measurements⁴⁰. In the Mott phase of clean 1T-TaS₂ the

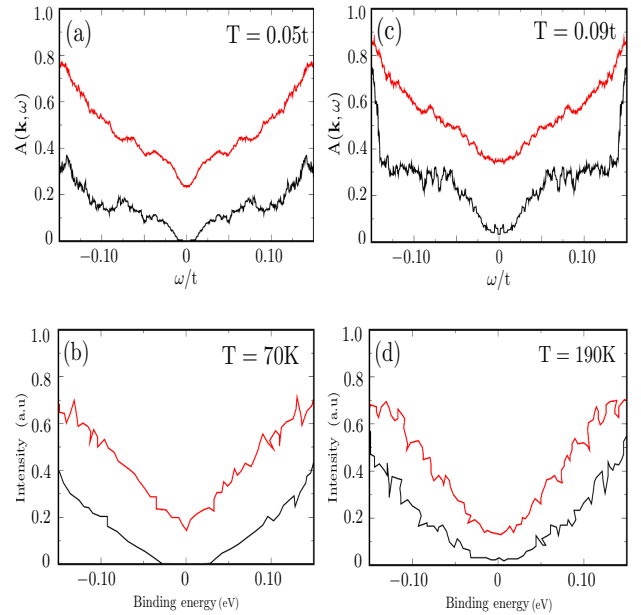


FIG. 9. Color online: Temperature dependence of numerically determined spectral lineshape (a) and (c) and experimental EDC (b) and (d), for the clean (black) and disordered (red) system. At low temperature the spectra is gapped out for the clean system while in presence of disorder there is a soft gap at the Fermi level. Temperature leads to monotonic closure of the gap via thermal fluctuations induced suppression of (quasi) long range angular correlation between the magnetic moments. Both the experimental and numerical data are symmetrized and for the numerical calculations the results correspond to $W = 1.75t$. The experimental data is extracted from Ref.⁴⁰.

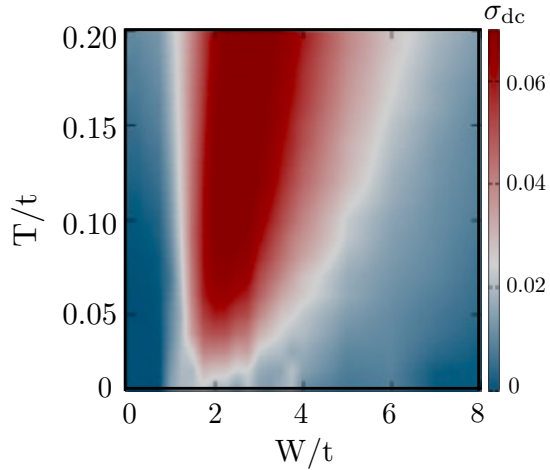


FIG. 10. Color online: Disorder stabilized NFL metal in the disorder-temperature ($W - T$)-plane depicted in terms of the σ_{dc} . The large conductivity at intermediate disorder regime (AFM) attests the metallic phase, while for the AF-MI and CAI regime at weak and strong disorder, respectively, the conductivity is strongly suppressed. Generic features of disorder tuned IMT shown in this figure can be compared with the experimental observations of applied electric field controlled interaction tuned IMT in 2D TMD frustrated Mott insulators³².

band lying closest to the Fermi energy has a bandwidth $W_B \approx 45\text{meV}$, while the onsite Coulomb energy is found to be of the order of $\approx 0.1\text{eV}$ ³⁷. Accordingly, $U/W_B \approx 2.2$, which is larger than $U_c/W_B \approx 1.3$ corresponding to the Mott transition and the system is well within the Mott insulating phase⁸³. In the clean limit the single band Hubbard model on a triangular lattice is in the Mott insulating phase beyond $U_c \approx 5.27t$ ⁴⁹. Our choice of $U = 6t$ in this work thus ensures that we are in the experimentally relevant regime for our numerical calculations.

The energy distribution curve (EDC) at the Γ -point of the Brillouin zone, as obtained from the ARPES measurements reveal that disorder leads to accumulation of spectral weight at the Fermi level and gives rise to pseudogap. The experimentally observed EDC at the Γ -point for clean and Cu intercalated 1T-TaS₂ are shown in Figure 8(a)⁴⁰. For comparison we show the low temperature spectral lineshape $A(\mathbf{k}, \omega)$ at the Γ -point, obtained numerically, in Figure 8(b). The disorder generated pseudogap at the Fermi level is in excellent agreement with the experimental observations. Thermal fluctuations lead to progressive closure of the pseudogap, accompanying the crossover of the system from the NFL to bad metallic phase, as is observed both experimentally as well as from our numerical calculations, is shown in Figure 9.

IMT and the associated NFL behavior discussed in this paper is a fairly generic feature of 2D TMDs. Recently signatures of NFL have been realized in TMD heterostructures such as, MoTe₂/WSe₂ Moire superlattices³² and twisted bilayer WSe₂³³. In Ref.³² continuous insulator-metal transition is realized in MoTe₂/WSe₂ Moire heterostructure at half fill-

ing via applied electric field tuned electronic interaction. The corresponding resistivity measurements show deviation from T^2 behavior thereby providing clear signature of NFL physics. The thermal phase diagram of this system as mapped out in the electric field-temperature ($E - T$)-plane in terms of the electrical resistance shows that a metallic phase is stabilized close to the QCP (see Figure 3(c) of Ref.³²). The high temperature regime exhibits a crossover to the bad metallic phase. Moreover, magnetic susceptibility measurements confirmed the absence of long range magnetic order and/or presence of spiral antiferromagnetic order in this system at low temperatures. Notably, the loss of magnetic correlations is distinct from the IMT and gives rise to two different QCPs.

We establish the agreement of our results with the experimental observations reported in Ref.³² in terms of Figure 10 (to be compared with Figure 3(c) of Ref.³²), wherein we map out the thermal phase diagram in the $W - T$ plane in terms of the dc conductivity σ_{dc} . The generic features captured by our calculations are in excellent agreement with those of the experimental observations on 2D TMD. This allows us to conclude that the numerical approach used in our work is versatile and is suitable to capture the generic features of IMT in 2D frustrated Mott insulators.

Note that the IMT and the emergent NFL metal are closely related to the spatial inhomogeneity of the underlying phase. The role of spatial inhomogeneity was brought into focus by the advent of imaging techniques with nanoscale resolution, the most compelling example being VO₂⁸⁴. Near field infrared scanning spectroscopy on VO₂ thin films and microcrystals showed spatial proliferation of metallic and insulating “puddles” in presence of disorder, arising out of local fluctuations⁸⁴⁻⁸⁷. The corresponding transport signatures are expectedly non trivial as the scattering properties now vary locally.

Theoretical investigation of this rather complex phenomena of IMT requires one to take into account the fluctuations originating from disorder and thermal effects, a goal most of the powerful numerical techniques fail to achieve. In a recent work, an extension of DMFT technique (statistical-DMFT) has been employed to address this issue on a square lattice, at finite temperatures²⁴. Geometric frustration further complicates the problem since standard numerical techniques such as DQMC cannot be used owing to the fermionic sign problem, while the Hartree-Fock mean field theory by construction is applicable at $T = 0$ only. Our work presented in this paper provides an efficient numerical tool at reasonable computational expense. Access to large system sizes, real space correlators and real frequency dependent properties provide the edge to our approach over the existing ones.

In conclusion, we for the first time have provided the microscopic description of the disorder stabilized metal in 2D frustrated Mott insulators. Based on a non perturbative numerical technique we have mapped out the phases and the relevant thermal scales, exhibiting a disorder induced Mott insulator-metal transition. By analyzing the phases based on the thermodynamic, spectroscopic and transport signatures we have shown that the emergent metal is a non Fermi liquid, characterized by resilient quasiparticles and undergoes ther-

mal crossover to bad metallic phase. As a test case for our approach we selected Cu intercalated 1T-TaS₂, which is a 2D transition metal dichalcogenide Mott insulator. Our results are in excellent agreement with the existing experimental observations on this material and are expected to serve as benchmarks for future experiments on this and related class of materials. Further, we demonstrated that the signatures of IMT in 2D frustrated Mott insulators are fairly generic and is well captured by our numerical approach.

V. ACKNOWLEDGEMENTS:-

The authors would like to thank the high performance computing cluster (HPCC) facility at Harish Chandra Research institute, Prayagraj (Allahabad), India.

VI. APPENDIX

A. Numerical approach

The Anderson-Hubbard model on a triangular lattice reads as⁸,

$$H = \sum_{\langle ij \rangle, \sigma} t_{ij} (c_{i\sigma}^\dagger c_{j\sigma} + h.c.) + \sum_{i, \sigma} (W_i - \mu) \hat{n}_{i\sigma} + U \sum_i \hat{n}_{i\uparrow} \hat{n}_{i\downarrow}$$

here, $t_{ij} = -t$ for the nearest neighbor hopping on an isotropic triangular lattice. $t = 1$ is set as the reference energy scale. $U > 0$ is the on-site repulsive Hubbard interaction. The site dependent disorder is introduced in the system via W_i which is randomly selected from a uniform distribution $[+W/2, -W/2]$. We work at half filling and the chemical potential μ is adjusted to achieve the same. In order to make the model numerically tractable we decompose the interaction term using Hubbard Stratonovich (HS) decomposition^{56,57} and thereby introduce two (bosonic) auxiliary fields viz. a vector field $\mathbf{m}_i(\tau)$ and a scalar field $\phi_i(\tau)$, which couples to the spin and charge densities, respectively. The introduction of these auxiliary fields aid in to capture the Hartree-Fock theory at the saddle point, retains the spin rotation invariance and the Goldstone modes. In terms of the Grassmann fields $\psi_{i\sigma}(\tau)$, we have,

$$\exp \left[U \sum_i \bar{\psi}_{i\uparrow} \psi_{i\uparrow} \bar{\psi}_{i\downarrow} \psi_{i\downarrow} \right] = \int \prod_i \frac{d\phi_i d\mathbf{m}_i}{4\pi^2 U} \exp \left[\frac{\phi_i^2}{U} + i\phi_i \rho_i + \frac{m_i^2}{U} - 2\mathbf{m}_i \cdot \mathbf{s}_i \right] \quad (8)$$

where, the charge and spin densities are defined as, $\rho_i = \sum_{\sigma} \bar{\psi}_{i\sigma} \psi_{i\sigma}$ and $\mathbf{s}_i = (1/2) \sum_{a,b} \bar{\psi}_{i\sigma} \sigma_{ab} \psi_{i\sigma}$, respectively. The corresponding partition function thus takes the form,

$$\mathcal{Z} = \int \prod_i \frac{d\bar{\psi}_{i\sigma} d\psi_{i\sigma} d\phi_i d\mathbf{m}_i}{4\pi^2 U} \exp \left[- \int_0^\beta \mathcal{L}(\tau) \right] \quad (9)$$

where, the Lagrangian \mathcal{L} is defined as,

$$\begin{aligned} \mathcal{L}(\tau) = & \sum_{i\sigma} \bar{\psi}_{i\sigma}(\tau) \partial_\tau \psi_{i\sigma}(\tau) + H_0(\tau) \\ & + \sum_i \left[\frac{\phi_i(\tau)^2}{U} + (i\phi_i(\tau) + W_i - \mu) \rho_i(\tau) + \frac{m_i(\tau)^2}{U} \right. \\ & \left. - 2\mathbf{m}_i(\tau) \cdot \mathbf{s}_i(\tau) \right] \end{aligned} \quad (10)$$

where, $H_0(\tau)$ is the kinetic energy contribution. The ψ integral is now quadratic but at the cost of an additional integration over the fields $\mathbf{m}_i(\tau)$ and $\phi_i(\tau)$. The weight factor for the \mathbf{m}_i and ϕ_i configurations can be determined by integrating out the ψ and $\bar{\psi}$; and using these weighted configurations one goes back and computes the fermionic properties. Formally,

$$\mathcal{Z} = \int \mathcal{D}\mathbf{m} \mathcal{D}\phi e^{-S_{eff}(\mathbf{m}, \phi)} \quad (11)$$

$$S_{eff} = \log \text{Det}[\mathcal{G}^{-1}\{\mathbf{m}, \phi\}] + \frac{\phi_i^2}{U} + \frac{m_i^2}{U} \quad (12)$$

where, \mathcal{G} is the electron Green's function in a $\{\mathbf{m}_i, \phi_i\}$ background.

The weight factor for an arbitrary space-time configuration $\{\mathbf{m}_i(\tau), \phi_i(\tau)\}$ involves computation of the fermionic determinant in that background. The auxiliary field quantum Monte Carlo with static path approximation (SPA) retains the full spatial dependence in \mathbf{m}_i and ϕ_i but keeps only the $\Omega_n = 0$ mode. It thus includes classical fluctuations of arbitrary magnitudes but no quantum ($\Omega_n \neq 0$) fluctuations.

Following the SPA approach, we freeze $\phi_i(\tau)$ to its saddle point value $\phi_i(\tau) = \langle n_i \rangle U/2 = U/2$ (at half filling). Note that this approximation is valid strictly at half filling where the charge fluctuations are suppressed, for large U . Away from half filling, the charge fluctuations would be large even for large U . The resulting model can be thought of as fermions coupled to spatially fluctuating random background of classical field \mathbf{m}_i . With these approximations the effective Hamiltonian corresponds to a coupled spin-fermion model, which reads as,

$$\begin{aligned} H_{eff} = & \sum_{\langle ij \rangle, \sigma} t_{ij} [c_{i\sigma}^\dagger c_{j\sigma} + h.c.] + \sum_{i\sigma} \left(\frac{U}{2} + W_i - \mu \right) \hat{n}_{i\sigma} \\ & - \frac{U}{2} \sum_i \mathbf{m}_i \cdot \sigma_i + \frac{U}{4} \sum_i m_i^2 \end{aligned} \quad (13)$$

where, the last term corresponds to the stiffness cost associated with the now classical field \mathbf{m}_i and $\sigma_i = \sum_{a,b} c_{ia}^\dagger \sigma_{ab} c_{ib} = \mathbf{s}_i$.

The random background configurations of $\{\mathbf{m}_i\}$ are generated numerically via Monte Carlo simulation and obey the Boltzmann distribution,

$$P\{\mathbf{m}_i\} \propto \text{Tr}_{c,c^\dagger} e^{-\beta H_{eff}} \quad (14)$$

For large and random configurations the trace is computed numerically, wherein we diagonalize H_{eff} for each attempted

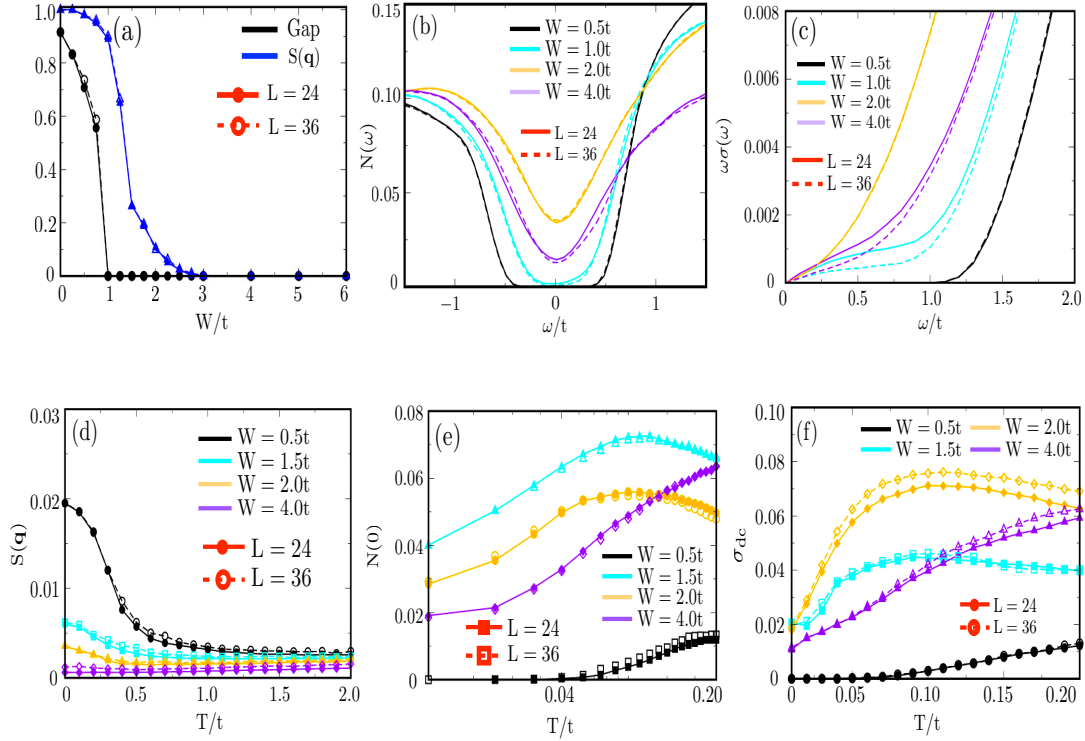


FIG. 11. Color online: Comparison of indicators at the ground state and at finite temperatures as calculated on system sizes of $L = 36$ (dashed lines) and $L = 24$ (solid lines). The panels correspond to, (a) Mott gap and magnetic structure factor peak at $T = 0$, (b) single particle DOS ($N(\omega)$) for different W/t at $T = 0$, (c) scaled optical conductivity ($\omega\sigma(\omega)$) in the low frequency regime for different W/t at $T = 0$, (d) temperature dependence of magnetic structure factor peak at $\mathbf{q} = \{2\pi/3, 2\pi/3\}$ for selected W/t , (e) temperature dependence of single particle DOS ($N(0)$) at the Fermi level for different W/t , (f) temperature dependence of dc conductivity (σ_{dc}) at selected W/t .

update of \mathbf{m}_i and converge to the equilibrium configuration using Metropolis algorithm. Evidently, the process is numerically expensive and involves an $O(N^3)$ computational cost per update (where $N = L \times L$ correspond to the system size), thus the cost per MC sweep is N^4 . We cut down on the computation by using travelling cluster algorithm, wherein instead of diagonalizing the entire lattice for each attempted update of \mathbf{m}_i we diagonalize a smaller cluster surrounding the update site⁸⁸. The computation cost now scales as $O(NN_c^3)$ (where N_c is the size of a smaller cluster surrounding the update site), which is linear in lattice size N . This allows us to access large system sizes $\sim 40 \times 40$ in two dimensions, which is essential to capture the inhomogeneity of the underlying magnetic phase. The equilibrium configurations obtained via the combination of Monte Carlo and Metropolis at different temperatures are used to compute the different fermionic correlators.

SPA does not take into account the effect of quantum fluctuations. We do not expect a qualitative change in the results reported in this manuscript in case quantum fluctuations are considered. For a clean system a *possible* consequence of taking into account the effect of quantum fluctuations is the restoration of the translation invariance of the lattice in the metallic phase. This is expected to make the metallic phase perfectly conducting at $T=0$ and above a low coherence tem-

perature, signatures of a highly resistive metal would be observed. Inclusion of disorder in the system eliminates such a possibility because the translation symmetry of the lattice is anyway broken by disorder and cannot be restored by quantum fluctuations. In the presence of disorder spatial fluctuations play a vital role at finite temperatures.

Static path approximation has been used to investigate several quantum many body phenomena, such as, BCS-BEC crossover in superconductors⁸⁹, Fulde-Ferrell-Larkin-Ovchinnikov (FFLO) superconductivity in solid state systems and ultracold atomic gases⁵², Mott transition in frustrated lattices^{49-51,90}, d-wave superconductivity⁹¹, competition and coexistence of magnetic (AFM) and d-wave superconducting orders⁹², orbital selective magnetism relevant for iron superconductors⁹³, strain induced superconductor-insulator transition in flat band lattices⁵⁴, heteromolecular ultracold atomic gases⁵³ etc. In many of these problems the use of numerically exact techniques like DQMC is not feasible due either to the sign problem or to the system size restrictions (particularly for multiband systems). Judicial approximations are thus essential and SPA is one such approximation which can capture the ground state and thermal properties of these strongly correlated systems with reasonable accuracy. The technique however will and does fall short in situations

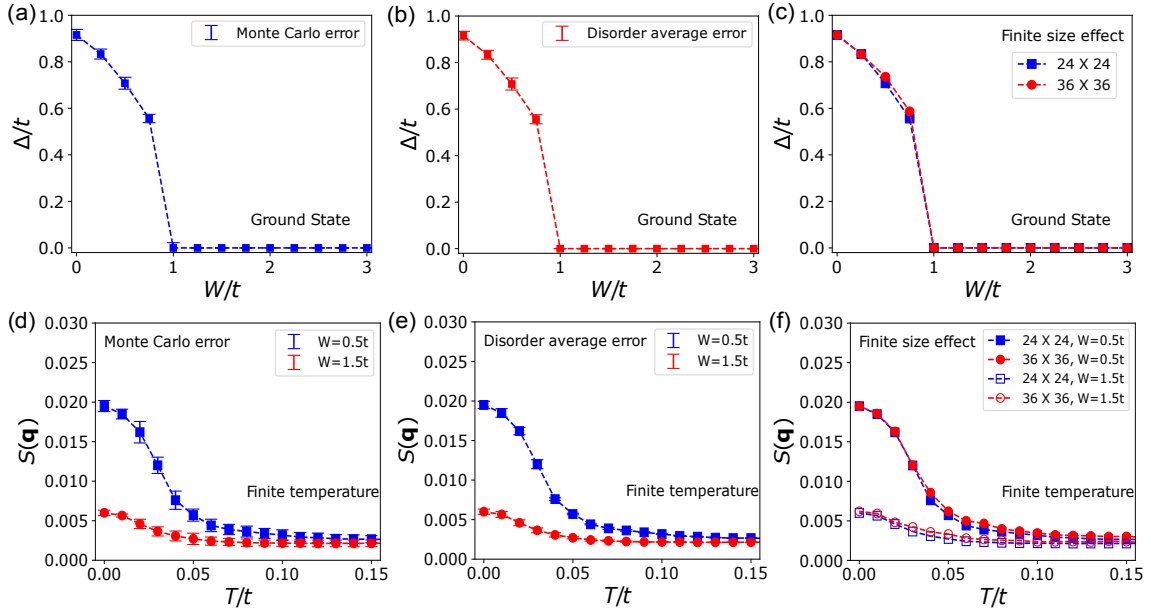


FIG. 12. Color online: Numerical error for representative indicators at the ground state and at finite temperatures, as selected disorder potentials. The error arising out of Monte Carlo sampling, disorder averaging and finite system size effects, are shown as separate panels, for the ground state and finite temperature indicators.

where the physics of the ground state is almost entirely dictated by quantum fluctuations, such as, quantum spin liquids, heavy fermion superconductors etc.

B. Finite system size effect

The results discussed in the manuscript corresponds to a system size of 24×24 . The choice of the system size is dictated by a balance between the computation cost and stability of the results obtained. Any lattice based simulation is however liable to be plagued by finite system size effects and in order to ascertain the robustness of our results against system sizes we have carried out the computation for selected disorder cross sections at a larger system size of 36×36 . In Figure 11 we show for the key indicators, the comparison between the results obtained for $L = 24$ and $L = 36$. We infer that our results are robust against the finite system size effects, both at the ground state and at finite temperatures.

In Figure 12, we systematically show the numerical error for the representative indicators at the ground state and at finite temperatures, arising out of, (a) Monte Carlo sampling, (b) disorder averaging and (c) finite system size effect. The data presented in our manuscript are averaged over 200 Monte Carlo configurations and 30 disorder realizations. In Figure 12, as the ground state indicator we show the disorder dependence of the Mott gap (Δ/t), while as the finite temperature indicator the temperature dependence of the magnetic structure factor peak $S(\mathbf{q})$ is presented at the selected disorder potential of $W = 0.5t$ and $W = 1.5t$. We have compared our results obtained at $L = 24$ with those obtained at $L = 36$, so as to ascertain the robustness of the thermodynamic phases and

the phase boundaries shown in the manuscript. In principle, even larger system sizes can be accessed with our numerical approach but that involves larger computation cost.

Our results for the ground state and finite temperature indicators show that within our numerical scheme the largest contribution to numerical error comes from the Monte Carlo sampling, followed by the contribution from disorder averaging. For both contributions the errorbars are comparable to the size of the data points and it can be further reduced by averaging over a larger number of Monte Carlo samples and disorder realizations, respectively. Over the regime of weak and intermediate disorder potential our results are robust against finite system size effects. Figure 12 shows that our choice of $L = 24$ is sufficiently large to eliminate errors arising out of finite system sizes.

C. First order phase transition and hysteresis

We have shown in the main text that at the ground state the disorder tuned Mott insulator-metal transition is weakly first order in nature. The same has been depicted in term of the Mott gap as determined from the single particle DOS (see Figure 2(a) in the main text). An additional confirmation of the weak first order nature of this phase transition is obtained from the hysteresis behavior that the Mott gap shows as function of increasing and decreasing disorder, as presented in Figure 13.

In order to verify the hysteresis of the spectral gap at the Fermi level we begin with the equilibrium configuration of the classical fields in the clean limit at the low temperature and subject it to a random disorder configuration with dis-

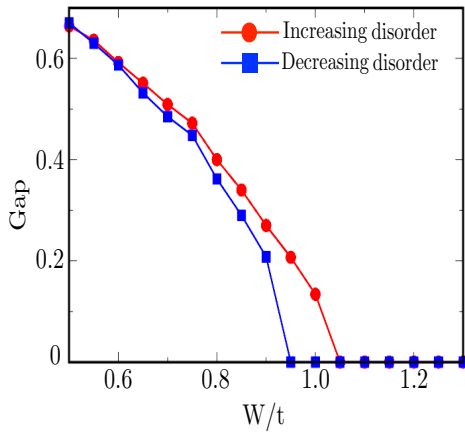


FIG. 13. Color online: Weakly first order phase transition of the Mott gap across the Mott insulator-metal transition. With increasing disorder the gap closes at $W = 1.05t$ while with decreasing disorder it closes at $W = 0.95t$.

order potential strength W . A random number seed is used to generate this disorder configuration. The strength of the disorder potential is then progressively increased in steps of $\Delta W = 0.05t$ upto $W = 3t$, while keeping the random number seed to be the same. A particular choice of random number seed corresponds to a single disorder realization. The process is repeated with different random number seeds (thus different disorder realizations) and for each realization the single particle DOS is calculated, which are then averaged over the disorder realizations. The averaged single particle DOS is used to determine the spectral gap at the Fermi level, as function of increasing disorder strength.

Next, we consider the final equilibrium configuration of the classical fields at $W = 3t$ for a single disorder realization as the input and progressively reduce the strength of the disorder potential in steps of $\Delta W = 0.05t$ till it reaches the clean limit. This process is repeated using the final equilibrium configurations of the classical fields at $W = 3t$ for different disorder realizations. The disorder averaged single particle DOS for different disorder strength is then calculated and the corresponding spectral gap at the Fermi level is determined, as function of decreasing disorder strength.

* madhuparna.k@gmail.com

† nyayabanta@nus.edu.sg

¹ E. Abrahams, S. V. Kravchenko, and M. P. Sarachik, *Rev. Mod. Phys.* **73**, 251 (2001).

² S. V. Kravchenko and M. P. Sarachik, *Reports on Progress in Physics* **67**, 1 (2003).

³ N. T. V. Dobrosavljević and J. Valle, *Conductor-Insulator Quantum Phase Transitions* (Oxford University Press, New York, 2012).

⁴ P. W. Anderson, *Phys. Rev.* **109**, 1492 (1958).

⁵ E. Abrahams, P. W. Anderson, D. C. Licciardello, and T. V. Ramakrishnan, *Phys. Rev. Lett.* **42**, 673 (1979).

⁶ N. F. Mott, *Metal-Insulator Transitions* (Taylor and Francis, 1990).

⁷ N. F. Mott, *Proceedings of the Physical Society. Section A* **62**, 416 (1949).

⁸ P. Fazekas, *Lecture Notes on Electron Correlation and Magnetism* (World Scientific, Singapore, 1999).

⁹ A. M. Finkel'stein, *Zh. Eksp. Teor. Fiz.* **84**, 168 (1983).

¹⁰ A. M. Finkel'stein, *Pis'ma Zh. Eksp. Teor. Fiz.* **37**, 436 (1983).

¹¹ S. V. Kravchenko, G. V. Kravchenko, J. E. Furneaux, V. M. Pudalov, and M. D'Iorio, *Phys. Rev. B* **50**, 8039 (1994).

¹² D. Heidarian and N. Trivedi, *Phys. Rev. Lett.* **93**, 126401 (2004).

¹³ J. C. Szabo, K. Lee, V. Madhavan, and N. Trivedi, *Phys. Rev. Lett.* **124**, 137402 (2020).

¹⁴ K. Byczuk, W. Hofstetter, and D. Vollhardt, *Phys. Rev. Lett.* **94**, 056404 (2005).

¹⁵ M. Aguiar, V. Dobrosavljević, E. Abrahams, and G. Kotliar, *Physica B: Condensed Matter* **403**, 1417 (2008).

¹⁶ W. S. Oliveira, M. C. O. Aguiar, and V. Dobrosavljević, *Phys. Rev. B* **89**, 165138 (2014).

¹⁷ M. C. O. Aguiar, V. Dobrosavljević, E. Abrahams, and G. Kotliar, *Phys. Rev. Lett.* **102**, 156402 (2009).

¹⁸ D. Semmler, K. Byczuk, and W. Hofstetter, *Phys. Rev. B* **81**, 115111 (2010).

¹⁹ D. Tanasković, V. Dobrosavljević, E. Abrahams, and G. Kotliar,

Phys. Rev. Lett. **91**, 066603 (2003).

²⁰ H. Lee, H. O. Jeschke, and R. Valentí, *Phys. Rev. B* **93**, 224203 (2016).

²¹ Y. Song, R. Wortis, and W. A. Atkinson, *Phys. Rev. B* **77**, 054202 (2008).

²² T. Ohashi, T. Momoi, H. Tsunetsugu, and N. Kawakami, *Phys. Rev. Lett.* **100**, 076402 (2008).

²³ A. Liebsch, H. Ishida, and J. Merino, *Phys. Rev. B* **79**, 195108 (2009).

²⁴ M. Y. Suárez-Villagrán, N. Mitsakos, T.-H. Lee, V. Dobrosavljević, J. H. Miller, and E. Miranda, *Phys. Rev. B* **101**, 235112 (2020).

²⁵ B. Srinivasan, G. Benenti, and D. L. Shepelyansky, *Phys. Rev. B* **67**, 205112 (2003).

²⁶ Y. Otsuka and Y. Hatsugai, *Journal of Physics: Condensed Matter* **12**, 9317 (2000).

²⁷ S. Chiesa, P. B. Chakraborty, W. E. Pickett, and R. T. Scalettar, *Phys. Rev. Lett.* **101**, 086401 (2008).

²⁸ R. Kotlyar and S. Das Sarma, *Phys. Rev. Lett.* **86**, 2388 (2001).

²⁹ H. Bragança, M. C. O. Aguiar, J. Vučičević, D. Tanasković, and V. Dobrosavljević, *Phys. Rev. B* **92**, 125143 (2015).

³⁰ C. E. Ekuma, S.-X. Yang, H. Terletska, K.-M. Tam, N. S. Vidhyadhiraja, J. Moreno, and M. Jarrell, *Phys. Rev. B* **92**, 201114 (2015).

³¹ N. D. Patel, A. Mukherjee, N. Kaushal, A. Moreo, and E. Dagotto, *Phys. Rev. Lett.* **119**, 086601 (2017).

³² T. Li, S. Jiang, L. Li, Y. Zhang, K. Kang, J. Zhu, K. Watanabe, T. Taniguchi, D. Chowdhury, L. Fu, J. Shan, and K. F. Mak, (2021), [arXiv:2103.09779](https://arxiv.org/abs/2103.09779) [cond-mat.str-el].

³³ A. Ghiotto, E.-M. Shih, G. S. S. G. Pereira, D. A. Rhodes, B. Kim, J. Zang, A. J. Millis, K. Watanabe, T. Taniguchi, J. C. Hone, L. Wang, C. R. Dean, and A. N. Pasupathy, (2021), [arXiv:2103.09796](https://arxiv.org/abs/2103.09796) [cond-mat.mes-hall].

³⁴ P. Fazekas and E. Tosatti, *Physica B+C* **99**, 183 (1980).

³⁵ K. Aryanpour, W. E. Pickett, and R. T. Scalettar,

- Phys. Rev. B **74**, 085117 (2006).
- 36 J. Wilson, F. D. Salvo, and S. Mahajan, *Advances in Physics* **24**, 117 (1975).
 - 37 B. Sipos, A. F. Kusmartseva, A. Akrap, H. Berger, L. Forr, and E. TutiÅ, *Nature Materials* **7**, 960 (2008).
 - 38 P. Xu, J. O. Piatek, P.-H. Lin, B. Sipos, H. Berger, L. Forró, H. M. Rønnow, and M. Grioni, *Phys. Rev. B* **81**, 172503 (2010).
 - 39 X.-Y. Zhu, S. Wang, Z.-Y. Jia, L. Zhu, Q.-Y. Li, W.-M. Zhao, C.-L. Xue, Y.-J. Xu, Z. Ma, J. Wen, S.-L. Yu, J.-X. Li, and S.-C. Li, *Phys. Rev. Lett.* **123**, 206405 (2019).
 - 40 E. Lahoud, O. N. Meetei, K. B. Chaska, A. Kanigel, and N. Trivedi, *Phys. Rev. Lett.* **112**, 206402 (2014).
 - 41 Q. Niu, W. Zhang, Y. T. Chan, E. C. T. O'Farrell, R. Doganov, K. Y. Yip, K. T. Lai, W. C. Yu, B. Özyilmaz, G. R. Stewart, J. S. Kim, and S. K. Goh, *Phys. Rev. Research* **2**, 023297 (2020).
 - 42 S.-H. Lee, J. S. Goh, and D. Cho, *Phys. Rev. Lett.* **122**, 106404 (2019).
 - 43 J. Skolimowski, Y. Gerasimenko, and R. Žitko, *Phys. Rev. Lett.* **122**, 036802 (2019).
 - 44 L. Balents, *Nature* **464**, 199 (2010).
 - 45 R. Yamamoto, T. Furukawa, K. Miyagawa, T. Sasaki, K. Kanoda, and T. Itou, *Phys. Rev. Lett.* **124**, 046404 (2020).
 - 46 W. E. Evenson, J. R. Schrieffer, and S. Q. Wang, *Journal of Applied Physics* **41**, 1199 (1970).
 - 47 Y. Dubi, Y. Meir, and Y. Avishai, *Nature* **449**, 876 (2007).
 - 48 S. Tarat and P. Majumdar, *EPL (Europhysics Letters)* **105**, 67002 (2014).
 - 49 R. Tiwari and P. Majumdar, (2013), arXiv:1301.5026.
 - 50 N. Swain, R. Tiwari, and P. Majumdar, *Phys. Rev. B* **94**, 155119 (2016).
 - 51 N. Swain and P. Majumdar, *Journal of Physics: Condensed Matter* **29**, 085603 (2017).
 - 52 M. Karmakar and P. Majumdar, *Phys. Rev. A* **93**, 053609 (2016).
 - 53 M. Karmakar, *Phys. Rev. A* **97**, 033617 (2018).
 - 54 N. Swain and M. Karmakar, *Phys. Rev. Research* **2**, 023136 (2020).
 - 55 P. J. H. Denteneer, R. T. Scalettar, and N. Trivedi, *Phys. Rev. Lett.* **83**, 4610 (1999).
 - 56 J. Hubbard, *Phys. Rev. Lett.* **3**, 77 (1959).
 - 57 H. J. Schulz, *Phys. Rev. Lett.* **65**, 2462 (1990).
 - 58 H. Morita, S. Watanabe, and M. Imada, *Journal of the Physical Society of Japan* **71**, 2109 (2002).
 - 59 T. Watanabe, H. Yokoyama, Y. Tanaka, and J. Inoue, *Phys. Rev. B* **77**, 214505 (2008).
 - 60 T. Yoshioka, A. Koga, and N. Kawakami, *Phys. Rev. Lett.* **103**, 036401 (2009).
 - 61 L. F. Tocchio, A. Parola, C. Gros, and F. Becca, *Phys. Rev. B* **80**, 064419 (2009).
 - 62 P. Limelette, P. Wzietek, S. Florens, A. Georges, T. A. Costi, C. Pasquier, D. Jérôme, C. Mézière, and P. Batail, *Phys. Rev. Lett.* **91**, 016401 (2003).
 - 63 D. Galanakis, T. D. Stanescu, and P. Phillips, *Phys. Rev. B* **79**, 115116 (2009).
 - 64 O. Parcollet, G. Biroli, and G. Kotliar, *Phys. Rev. Lett.* **92**, 226402 (2004).
 - 65 T. Sato, K. Hattori, and H. Tsunetsugu, *Journal of the Physical Society of Japan* **81**, 083703 (2012).
 - 66 P. Sahebsara and D. Sénéchal, *Phys. Rev. Lett.* **100**, 136402 (2008).
 - 67 H.-Y. Yang, A. M. Läuchli, F. Mila, and K. P. Schmidt, *Phys. Rev. Lett.* **105**, 267204 (2010).
 - 68 K. Misumi, T. Kaneko, and Y. Ohta, *Phys. Rev. B* **95**, 075124 (2017).
 - 69 L. F. Tocchio, A. Montorsi, and F. Becca, *Phys. Rev. B* **102**, 115150 (2020).
 - 70 A. Wietek, R. Rossi, F. Šimkovic, M. Klett, P. Hansmann, M. Ferrero, E. Miles Stoudenmire, T. Schäfer, and A. Georges, (2021), arXiv:2102.12904.
 - 71 A. Pustogow, R. Rösslhuber, Y. Tan, E. Uykur, A. Böhme, M. Wenzel, Y. Saito, A. Löhle, R. Hübner, A. Kawamoto, J. A. Schlueter, V. Dobrosavljević, and M. Dressel, *npj Quantum Materials* **6**, 9 (2021).
 - 72 G. Moeller, V. Dobrosavljević, and A. E. Ruckenstein, *Phys. Rev. B* **59**, 6846 (1999).
 - 73 H. Park, K. Haule, and G. Kotliar, *Phys. Rev. Lett.* **101**, 186403 (2008).
 - 74 A. Casey, H. Patel, J. Nyéki, B. P. Cowan, and J. Saunders, *Phys. Rev. Lett.* **90**, 115301 (2003).
 - 75 Y. Imry, *Introduction to Mesoscopic Physics* (Oxford University Press on Demand, New York, 2002).
 - 76 N. D. Mermin and H. Wagner, *Phys. Rev. Lett.* **17**, 1133 (1966).
 - 77 O. Gunnarsson, M. Calandra, and J. E. Han, *Rev. Mod. Phys.* **75**, 1085 (2003).
 - 78 N. E. Hussey, K. Takenaka, and H. Takagi, *Philosophical Magazine* **84**, 2847 (2004).
 - 79 X. Deng, J. Mravlje, R. Žitko, M. Ferrero, G. Kotliar, and A. Georges, *Phys. Rev. Lett.* **110**, 086401 (2013).
 - 80 A. Pustogow, Y. Saito, A. Löhle, M. Sanz Alonso, A. Kawamoto, V. Dobrosavljević, M. Dressel, and S. Fratini, *Nature Communications* **12**, 1571 (2021).
 - 81 M. Urai, K. Miyagawa, T. Sasaki, H. Taniguchi, and K. Kanoda, *Phys. Rev. Lett.* **124**, 117204 (2020).
 - 82 E. C. Andrade, E. Miranda, and V. Dobrosavljević, *Phys. Rev. Lett.* **102**, 206403 (2009).
 - 83 K. Aryanpour, W. E. Pickett, and R. T. Scalettar, *Phys. Rev. B* **74**, 085117 (2006).
 - 84 M. M. Qazilbash, M. Brehm, B.-G. Chae, P.-C. Ho, G. O. Andreev, B.-J. Kim, S. J. Yun, A. V. Balatsky, M. B. Maple, F. Keilmann, H.-T. Kim, and D. N. Basov, *Science* **318**, 1750 (2007).
 - 85 M. M. Qazilbash, M. Brehm, G. O. Andreev, A. Frenzel, P.-C. Ho, B.-G. Chae, B.-J. Kim, S. J. Yun, H.-T. Kim, A. V. Balatsky, O. G. Shpyrko, M. B. Maple, F. Keilmann, and D. N. Basov, *Phys. Rev. B* **79**, 075107 (2009).
 - 86 B. T. O'Callahan, A. C. Jones, J. Hyung Park, D. H. Cobden, J. M. Atkin, and M. B. Raschke, *Nature Communications* **6**, 6849 (2015).
 - 87 M. K. Liu, M. Wagner, E. Abreu, S. Kittiwatanakul, A. McLeod, Z. Fei, M. Goldflam, S. Dai, M. M. Fogler, J. Lu, S. A. Wolf, R. D. Averitt, and D. N. Basov, *Phys. Rev. Lett.* **111**, 096602 (2013).
 - 88 Kumar, S. and Majumdar, P., *Eur. Phys. J. B* **50**, 571 (2006).
 - 89 S. Tarat and P. Majumdar, *The European Physical Journal B* **88**, 68 (2015).
 - 90 N. Swain and P. Majumdar, *Europhysics Letters* **119**, 17004 (2017).
 - 91 M. Mayr, G. Alvarez, C. Şen, and E. Dagotto, *Phys. Rev. Lett.* **94**, 217001 (2005).
 - 92 G. Alvarez, M. Mayr, A. Moreo, and E. Dagotto, *Phys. Rev. B* **71**, 014514 (2005).
 - 93 A. Mukherjee, N. D. Patel, A. Moreo, and E. Dagotto, *Phys. Rev. B* **93**, 085144 (2016).